



Direct-imaging Discovery and Dynamical Mass of a Substellar Companion Orbiting an Accelerating Hyades Sun-like Star with SCEXAO/CHARIS*

Masayuki Kuzuhara^{1,2}, Thayne Currie^{3,4,5}, Takuya Takarada^{1,2}, Timothy D. Brandt⁶, Bun'ei Sato⁷, Taichi Uyama³³, Markus Janson⁹, Jeffrey Chilcote¹⁰, Taylor Tobin¹⁰, Kellen Lawson¹¹, Yasunori Hori^{1,2,12}, Olivier Guyon^{1,3,13,14}, Tyler D. Groff¹⁵, Julien Lozi³, Sebastien Vievard³, Ananya Sahoo^{3,28}, Vincent Deo³, Nemanja Jovanovic¹⁶, Kyohoon Ahn³, Frantz Martinache¹⁷, Nour Skaf^{3,18}, Eiji Akiyama¹⁹, Barnaby R. Norris²⁰, Mickaël Bonnefoy²¹, Krzysztof G. Helminiak²², Tomoyuki Kudo³, Michael W. McElwain¹⁵, Matthias Samland²³, Kevin Wagner^{13,29}, John Wisniewski²⁴, Gillian R. Knapp²⁵, Jungmi Kwon²⁶, Jun Nishikawa^{1,2,12}, Eugene Serabyn²⁷, Masahiko Hayashi², and Motohide Tamura^{1,2,26}

¹ Astrobiology Center of NINS, 2-21-1, Osawa, Mitaka, Tokyo, 181-8588, Japan; m.kuzuhara@nao.ac.jp

² National Astronomical Observatory of Japan, 2-21-2, Osawa, Mitaka, Tokyo 181-8588, Japan

³ Subaru Telescope, National Astronomical Observatory of Japan, 650 North A'ohōkū Place, Hilo, HI 96720, USA

⁴ NASA-Ames Research Center, Moffett Boulevard, Moffett Field, CA, USA

⁵ Eureka Scientific, 2452 Delmer Street, Suite 100, Oakland, CA, USA

⁶ Department of Physics, University of California, Santa Barbara, California, USA

⁷ Department of Earth and Planetary Sciences, School of Science, Tokyo Institute of Technology, 2-12-1 Ookayama, Meguro-ku, Tokyo 152-8551, Japan

⁸ Infrared Processing and Analysis Center, California Institute of Technology, Pasadena, CA 91125, USA

⁹ Department of Astronomy, Stockholm University, Stockholm, Sweden

¹⁰ Department of Physics, University of Notre Dame, Notre Dame, IN, USA

¹¹ Homer S Dodge Department of Physics and Astronomy, University of Oklahoma, Norman, OK, USA

¹² Department of Astronomical Science, The Graduate University for Advanced Studies, SOKENDAI, 2-21-1 Osawa, Mitaka, Tokyo 181-8588, Japan

¹³ Steward Observatory, The University of Arizona, Tucson, AZ 85721, USA

¹⁴ College of Optical Sciences, University of Arizona, Tucson, AZ 85721, USA

¹⁵ NASA-Goddard Space Flight Center, Greenbelt, MD, USA

¹⁶ Department of Astronomy, California Institute of Technology, 1200 E. California Boulevard, Pasadena, CA 91125, USA

¹⁷ Université Côte d'Azur, Observatoire de la Côte d'Azur, CNRS, Laboratoire Lagrange, France

¹⁸ LESIA, Observatoire de Paris, Univ. PSL, CNRS, Sorbonne Univ., Univ. de Paris, 5 pl. Jules Janssen, F-92195 Meudon, France

¹⁹ Division of Fundamental Education and Liberal Arts, Department of Engineering, Niigata Institute of Technology 1719 Fujihashi, Kashiwazaki, Niigata 945-1195, Japan

²⁰ Sydney Institute for Astronomy, School of Physics, University of Sydney, Sydney, New South Wales, Australia

²¹ Université Grenoble Alpes, CNRS, IPAG, F-38000 Grenoble, France

²² Nicolaus Copernicus Astronomical Center of the Polish Academy of Sciences, ul. Rabińska 8, 87-100, Toruń, Poland

²³ Max-Planck-Institut für Astronomie, Königstuhl 17 D-69117, Heidelberg, Germany

²⁴ Department of Physics and Astronomy, University of Oklahoma, Norman, OK, USA

²⁵ Department of Astrophysical Science, Princeton University, Peyton Hall, Ivy Lane, Princeton, NJ 08544, USA

²⁶ Department of Astronomy, Graduate School of Science, The University of Tokyo, 7-3-1, Hongo, Bunkyo-ku, Tokyo, 113-0033, Japan

²⁷ Jet Propulsion Laboratory, California Institute of Technology, 4800 Oak Grove Drive, Pasadena, CA 91109, USA

²⁸ Space Telescope Science Institute, 3700 San Martin Drive, Baltimore, MD 21218, USA

²⁹ NASA Hubble Fellowship Program—Sagan Fellow

Received 2022 April 12; revised 2022 May 29; accepted 2022 June 9; published 2022 July 27

Abstract

We present the direct-imaging discovery of a substellar companion in orbit around a Sun-like star member of the Hyades open cluster. So far, no other substellar companions have been unambiguously confirmed via direct imaging around main-sequence stars in Hyades. The star HIP 21152 is an accelerating star as identified by the astrometry from the Gaia and Hipparcos satellites. We detected the companion, HIP 21152 B, in multiple epochs using the high-contrast imaging from SCEXAO/CHARIS and Keck/NIRC2. We also obtained the stellar radial-velocity data from the Okayama 188 cm telescope. The CHARIS spectroscopy reveals that HIP 21152 B's spectrum is consistent with the L/T transition, best fit by an early T dwarf. Our orbit modeling determines the semimajor axis and the dynamical mass of HIP 21152 B to be $17.5^{+7.2}_{-3.8}$ au and $27.8^{+8.4}_{-5.4} M_{\text{Jup}}$, respectively. The mass ratio of HIP 21152 B relative to its host is $\approx 2\%$, near the planet/brown dwarf boundary suggested by recent surveys. Mass estimates inferred from luminosity-evolution models are slightly higher ($33\text{--}42 M_{\text{Jup}}$). With a dynamical mass and a well-constrained age due to the system's Hyades membership, HIP 21152 B will become a critical benchmark in understanding the formation, evolution, and atmosphere of a substellar object as a function of mass and age. Our discovery is yet another key proof of concept for using precision astrometry to select direct-imaging targets.

* Based on data collected at Subaru Telescope, which is operated by the National Astronomical Observatory of Japan.

Unified Astronomy Thesaurus concepts: Brown dwarfs (185); Exoplanets (498); Open star clusters (1160); Direct imaging (387); Coronagraphic imaging (313); Astrometry (80); Exoplanet detection methods (489); Astronomical instrumentation (799)

1. Introduction

The direct-imaging (DI) technique is capable of detecting substellar companions with masses comparable to $\sim 1\text{--}20$ Jupiter masses (M_{Jup}) at projected separations wider than approximately 10 au, as demonstrated by discoveries such as the planets around HR 8799, β Pic, 51 Eri, PDS 70, and AB Aur (e.g., Marois et al. 2008; Lagrange et al. 2010; Macintosh et al. 2015; Keppler et al. 2018; Currie et al. 2022). However, extensive volume-/age-limited DI surveys have revealed a low ($<10\%$) occurrence rate for planet-mass companions (e.g., Nielsen et al. 2019).

Recent work shows the advantage of targeting stars that show evidence for the dynamical pull of a substellar companion, which provides a complementary approach to blind surveys. For example, targeted high-contrast imaging observations of the nearby Sun-like star HD 33632A from the Hipparcos-Gaia Catalogue of Accelerations (HGCA; Brandt 2018, 2021) have revealed a brown dwarf (BD) companion in the system (Currie et al. 2020a). The HGCA lists all nearby stars with significant proper-motion (PM) accelerations and allows to select promising targets for high-contrast imaging because the accelerated PM of a star can be caused by its companion. In addition, the HGCA is useful for analyzing the orbits of companions by combining it with DI data and/or radial-velocity (RV) measurements, often leading to a $\sim 10\%$ dynamical constraint on the companion's mass (e.g., Currie et al. 2020a; Bowler et al. 2021; Brandt et al. 2021). Thus, the use of HGCA also enables placing constraints on stellar and substellar evolution models by comparing the model-based mass of a companion with its dynamical mass measurement.

Imaged substellar companions around accelerating stars become even better benchmark objects if key system properties such as age and metallicity are well determined. The Hyades open cluster is one of the most extensively examined open clusters (OCs) in all of astronomy, with a thoroughly vetted membership list, well-constrained age, and well-determined metallicity (e.g., Brandt & Huang 2015; Gagné et al. 2018; Gossage et al. 2018). With typical distances of about 50 pc, Hyades members are near and bright enough that HGCA is well suited for identifying substellar companions.

We report the discovery of an L/T-transition BD companion around the accelerating star HIP 21152,³⁰ with the companions dynamical mass estimation. It is the first substellar companion directly imaged around a Sun-like star in the well-characterized Hyades OC and represents a new benchmark to better understand the properties of substellar objects.

2. HIP 21152 System Properties, Observations, and Data

HIP 21152 (HD 28736) is a nearby ($d = 43.208^{+0.050}_{-0.049}$ pc; Bailer-Jones et al. 2021) F5V star (Hoffleit 1964) with an

estimated mass of $\sim 1.3 M_{\odot}$ (David & Hillenbrand 2015). For this star, we first found a substantial deviation from simple linear kinematic motion (i.e., acceleration) from the HGCA based on Gaia DR2 (Brandt 2018). The updated measurement of acceleration in the HGCA based on Gaia EDR3 (Brandt 2021) is calculated to be $\chi^2 = 174.6$, consistent with a 13.0σ significance with two degrees of freedom (2 DOF). The Banyan- Σ (Gagné et al. 2018) algorithm³¹ provides HIP 21152 an extremely high membership probability (99.5%) for Hyades with the inputs from the Gaia EDR3 catalog (Gaia Collaboration et al. 2021). The age of Hyades OC was calculated to be 750 ± 100 Myr by Brandt & Huang (2015) and 676^{+67}_{-11} Myr³² by Gossage et al. (2018), taking stellar rotations into account.

2.1. SCExAO/CHARIS and Keck/NIRC2 High-contrast Imaging

We performed high-contrast imaging observations using adaptive optics (AO) on the Subaru and Keck II telescopes between 2020 October and 2021 October, in photometric and good-to-average seeing nights (Table 1). The Subaru observations utilized AO188 (Hayano et al. 2008) for first-stage correction of atmospheric turbulence, followed by a faster higher-order correction of residual wave-front errors by the extreme AO system SCExAO (Jovanovic et al. 2015; Currie et al. 2020b). A coronagraph within SCExAO is then deployed to mask the central starlight, yielding high-contrast images that are captured by the CHARIS integral field spectrograph (IFS; Groff et al. 2016). In our Keck observations, the target lights corrected by a near-IR Pyramid wave-front sensor were transferred to the NIRC2 camera (Bond et al. 2020).

The SCExAO/CHARIS and Keck/NIRC2 data obtained in 2020 have 55–98 minutes of on-source integration time. Our shallower SCExAO/CHARIS data set obtained in 2021 October aimed solely at rejecting the possibility that the companion candidate is a background object. All observations were performed in angular differential imaging (ADI) mode, and CHARIS's IFS also enabled spectral differential imaging (SDI; see Oppenheimer & Hinkley 2009 and references therein). All CHARIS data were taken with a low-resolution ($\mathcal{R} \sim 18$) spectroscopic mode to obtain wide wavelength coverage and the Lyot coronagraph with a $0''.23$ diameter mask; NIRC2 data were taken in the L' -band filter also using a Lyot coronagraph but with a larger ($0''.6$) mask (see Table 1). By modulating SCExAO's deformable mirror, we generated four satellite spots around the point-spread function (PSF) of HIP 21152 to enable astrometric and spectrophotometric calibration (e.g., Sahoo et al. 2020), while the NIRC2 coronagraph allows a direct stellar centroid estimate due to its partial transparency. To flux-calibrate the NIRC2 data, we obtained unsaturated PSFs of the star before and after the coronagraphic sequence.

Using the pipeline of Brandt et al. (2017), the raw CHARIS data were calibrated and converted into 2D image cubes consisting of 22 wavelength channels. To further process these

³⁰ The discovery of HIP 21152 B was independently reported by Bonavita et al. (2022) with their VLT/SPHERE imaging performed among a survey of a large sample of accelerating targets. K. Franson et al. (2022, in preparation) have also independently discovered HIP 21152 B with their originally obtained data and will characterize this system in detail with all the available data.

³¹ <http://www.exoplanetes.umontreal.ca/banyan/>

³² This is one of the six results in Gossage et al. (2018).

Table 1
HIP 21152 Observing Log and Companion Positions

UT Date (MJD ^a)	Instrument ^b	θ_v ($''$)	t_{exp} (s)	N_{exp}	ΔPar ($^{\circ}$)	Data Proc.	S/N	ρ (mas)	PA ($^{\circ}$)
2020-10-07 (59129.589)	SCEXAO/CHARIS	0.4–0.6	25.08	235	85.6	ADI	19.3	408.5 ± 4.5	217.40 ± 0.66
2020-12-04 (59187.445)	SCEXAO/CHARIS	0.5–0.7	25.08	131	62.6	ADI	15.8	401.4 ± 4.5	216.66 ± 0.69
2020-12-25 (59208.380)	PyWFS+NIRC2	0.5–0.6	60	65	60.7	ADI	10.7	406.2 ± 6.0	216.39 ± 0.85
2021-10-14 (59501.591)	SCEXAO/CHARIS	0.6–0.7	30.98	41	17.4	ASDI	10.0	378.7 ± 5.1	216.90 ± 0.79

Notes. θ_v represents the characteristic seeing measurements from the Canada–France–Hawaii Telescope seeing monitor. The integration time of each exposure, the numbers of exposures used in our analysis, and the total variation of the parallactic angle in each sequence are represented by t_{exp} , N_{exp} , and ΔPar , respectively. The column “Data Proc.” describes the types of our ALOCI PSF subtractions. S/N represents the companion PSFs’ signal-to-noise ratios calculated from the 22-channel collapsed images.

^a Center epochs (modified Julian days) during total exposure sequences.

^b The wavelength range for CHARIS is 1.16–2.37 μm , while the L' filter’s central wavelength for NIRC2 is 3.78 μm .

extracted data cubes, we used the CHARIS Data Processing Pipeline³³ following the outline in Currie et al. (2020b); the details of our high-contrast image processing are provided in Appendix A. The spectra of HIP 21152 A were measured with the satellite spots in each channel for spectrophotometric calibration, where we adopted an F5V model atmosphere from the Kurucz library (Castelli & Kurucz 2003) with the star’s 2MASS photometry (Skrutskie et al. 2006) as provided by IRSA (Skrutskie et al. 2003). The satellite spots are also used to register the central star’s PSFs to a common center. While the four spots have roughly equal brightnesses in each wavelength slice, the spot intensities for the 2020 December data showed a large systematic variation, making spectrophotometric calibration for these data more uncertain (see Appendix B.1). We processed the NIRC2 images using a well-tested pipeline (Currie et al. 2011, 2014) that carries out standard steps of sky subtraction, image registration, photometric calibration, and PSF subtraction. Our image processing primarily adopts the ALOCI algorithm for ADI PSF subtractions (e.g., Currie et al. 2014, 2018). We attempted additional processing to improve or validate the fiducial reductions using alternate ADI reductions that adopt the proprietary version of ALOCI and the SDI speckle suppression (see also Appendix A).

Figure 1 shows the HIP 21152 images obtained from our four data sets, from which HIP 21152 B is detected at signal-to-noise ratios³⁴ (S/Ns) of 10–19. We achieve comparable detections with the proprietary version of ALOCI, although the throughput of the proprietary version is far higher. SDI increases the S/N of the detection at the expense of greater spectroscopic uncertainty. To correct our spectrophotometry and astrometry for biasing due to processing, we carried out forward modeling as in previous work (Currie et al. 2018). The forward modeling on the ADI+SDI (ASDI) PSF subtraction accounts for the companion’s spectral type.

2.2. High-resolution Doppler Spectroscopy

We monitored HIP 21152 A with the high-efficiency fiber-link mode of the HIDES spectrograph equipped on the Okayama 188 cm telescope (HIDES-F; Kambe et al. 2013) to measure the star’s RVs. Our monitoring was conducted for about one year from 2011 December 30 and two years from 2020 February 11. In 2018 December, the spectrograph was

rearranged to improve the stability of RV measurements against temperature fluctuations. We used an image slicer, setting the spectral resolving power to be 55,000 by a 3.8 pixel sampling. The spectra of HIP 21152 passed through an I_2 cell, whose absorption features imposed on the spectra are used as references for RV calibration. Except for three poor-S/N (<30) spectra, we obtained 32 I_2 -imposed spectra of HIP 21152 A with integration times (IT) of 900 or 1800 s, and four I_2 -free spectra at various nights (IT = 1800×4 s). The I_2 -imposed spectra have S/Ns ranging from 57 to 258 at ≈ 5500 Å. Our RV calculations adopt a wavelength range from 5028 to 5753 Å, which contains numerous I_2 features and little telluric absorption. The data calibrations and extractions of one-dimensional spectra were performed in a standard way based on IRAF. The one-dimensional I_2 -free spectra are combined into a single-template spectrum after removing outliers and applying 3 pixel median smoothing³⁵ and barycentric correction to each spectrum. The same master template spectrum was compared with each of the 32 I_2 -imposed spectra to measure the RVs of HIP 21152 without producing an offset in the measurements. Our RV measurements were obtained using the pipeline of Sato et al. (2002, 2012), which corrects the line-profile fluctuations originating from the instrumental instability by modeling them from I_2 absorption lines. The spectra were divided into several segments with wavelength widths of ≈ 5.3 – 6.1 Å and the RVs were calculated in each segment. The wavelength widths of each segment were set to be much wider than standard RV measurements in HIDES because of HIP 21152’s rapid rotation. The adopted widths provide the smallest RV errors among several attempted segment widths. The segment-by-segment RVs were statistically summarized to be the final RV measurements in Appendix C.

3. Infrared Colors, Spectrum, and Atmosphere of HIP 21152 B

We base the following discussions on the 2020 October spectra (after correcting for spectrophotometry bias) presented in Appendix B.3 because the data at this epoch have the highest S/N, the most stable PSF quality, and the best calibration (see Appendix B.1). We calculated J , H , and K_s photometry from the 2020 October ADI spectrum using the bandpasses’ filter transmission profiles: $J = 17.72 \pm 0.20$, $H = 17.04 \pm 0.15$, and $K_s = 16.55 \pm 0.17$ mag. From NIRC2 data, we measure

³³ <https://github.com/thaynecurrie/charis-dpp>

³⁴ The S/Ns were calculated with the correction of Mawet et al. (2014).

³⁵ The broadening of absorption lines is limited by the star’s rapid rotation even after performing 3 pixel smoothing.

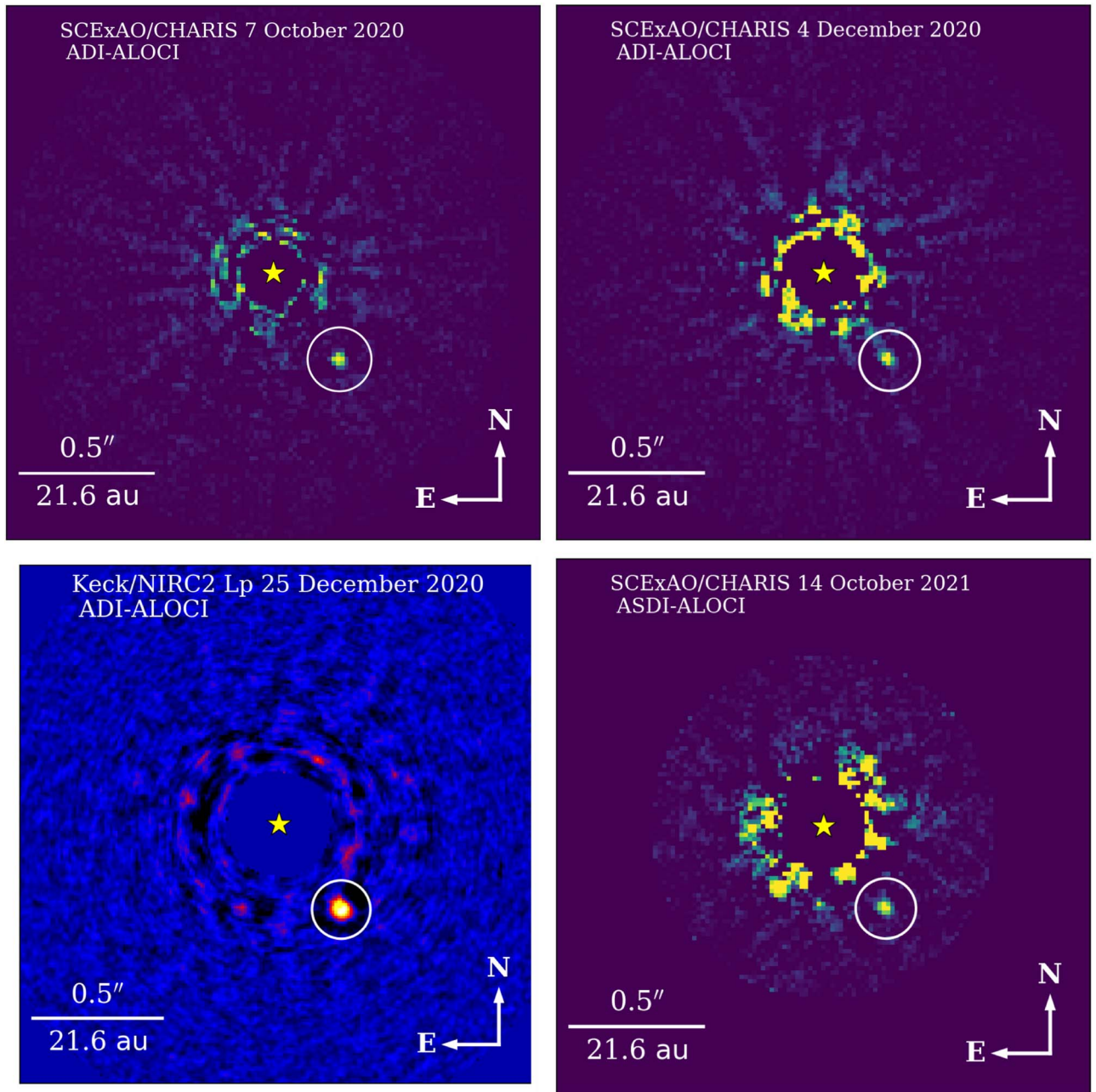


Figure 1. Images of HIP 21152 B (circled) detected from our SCEXAO/CHARIS and Keck/NIRC2 data. The areas close to the central star are masked.

$L' = 15.04 \pm 0.12$ for HIP 21152 B.³⁶ Figure 2 compares the near-infrared colors of HIP 21152 B to those of directly imaged BDs and young exoplanets. HIP 21152 B's colors are best reproduced by early T dwarfs, near the L–T transition, and are slightly bluer than HD 33632 Ab.

The extracted spectra of HIP 21152 B are shown in Figure 3, where we plot both the ADI and ASDI spectra as well as the ADI spectrum reduced with a proprietary code; measurements in each spectral channel agree among all reductions. HIP 21152 B's spectral shape shows strong absorption attributed to water opacity at the gaps between major near-infrared filters and a

³⁶ The companion's L' photometry was calibrated with HIP 21152 A's L' magnitude calculated from its 2MASS (Skrutskie et al. 2006) K_s -band photometry provided by IRSA (Skrutskie et al. 2003), the 2MASS color transformations from Carpenter (2001), and an F5-type star's $K-L$ color (0.04; Kenyon & Hartmann 1995).

very blue slope at $2.2\text{--}2.4 \mu\text{m}$ consistent with methane absorption.

To more quantitatively determine HIP 21152 B's spectral type, we performed a least-squares analysis by comparing the spectrum of HIP 21152 B with the template spectra of cool dwarfs (Currie et al. 2018). The template spectra were taken from the Montreal Spectral Library³⁷ (e.g., Gagné et al. 2015; Robert et al. 2016). We analyzed the 2020 October spectrum of HIP 21152 B obtained with the ADI-based PSF subtraction. The fit accounted for the spatially and spectrally correlated noise in an IFS spectrum using the scheme developed by Greco & Brandt (2016). We found that 95% of the off-diagonal elements of the spectral covariance were smaller than ≈ 0.16 at the companion's angular separation, indicating that the noise is

³⁷ <https://jgagneastro.com/the-montreal-spectral-library/>

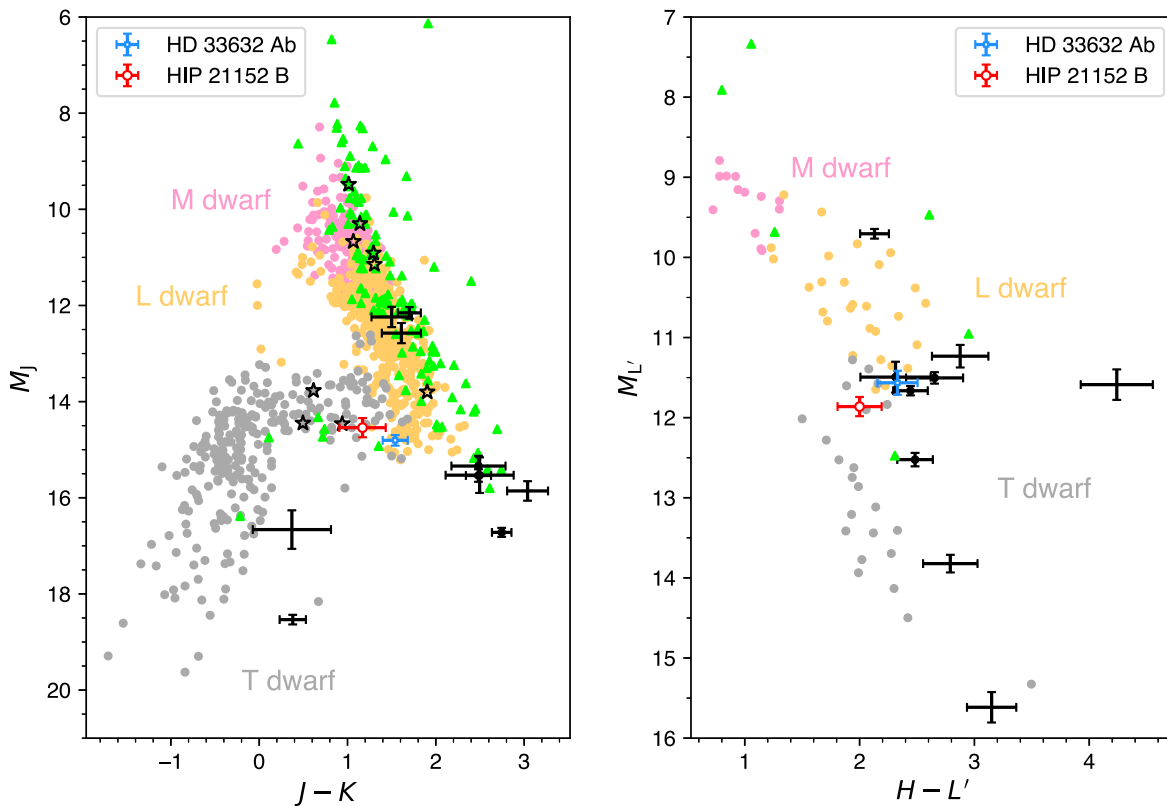


Figure 2. Color–magnitude diagram comparing HIP 21152 B (red open circle) to other substellar objects. (Left) $J - K$ vs. absolute J magnitude (M_J) and (right) $H - L'$ vs. absolute L' magnitude ($M_{L'}$). Triangle plots correspond to young or low surface-gravity MLT-type dwarfs. Some of the known representative substellar companions are shown by plots with 1σ error bars (data are from Dupuy & Liu 2012; Janson et al. 2013; Kuzuhara et al. 2013; De Rosa et al. 2016; Rajan et al. 2017; Best et al. 2020; Currie et al. 2020a); the planets around HR 8799 are indicated by the filled circles, which are made with the data from Marois et al. (2008), Metchev et al. (2009), Skemer et al. (2014), Currie et al. (2014), Zurlo et al. (2016), and the star’s 2MASS magnitudes (Skrutskie et al. 2006) from IRSA (Skrutskie et al. 2003). The distance–modulus values of the substellar companions are based on Bailer-Jones et al. (2021). All data of the MLT dwarfs are in the Maunakea Observatories passbands and taken from the compilations in Dupuy & Liu (2012), Leggett et al. (2010), and the database of Best et al. (2020). Star symbols represent the Hyades members (Banyan- Σ probabilities $>80\%$): photometry, parallax, and membership data are from Lodieu et al. (2019) and Best et al. (2020).

only weakly correlated both spatially and spectrally. The six wavelength channels affected by significant telluric absorption were omitted in the fit.

The χ^2 -based comparison shown in Figure 3 compares HIP 21152 B’s spectrum to the objects selected from the Montreal library. Overall, it is best fit by the T1.5-dwarf SIMP J2215+2210. Furthermore, the earlier-type template spectrum that best matches HIP 21152 B is the T0.5 object SIMP J1200–2836 ($\Delta\chi^2 \simeq 2$), while the later-type best match is T2 ($\Delta\chi^2 \simeq 2$; SIMP J1629+0335). Alternate ADI reductions find similar results. Earlier L-type dwarfs predict troughs in the water bands bracketing J , H , and K to be too shallow and have slopes in the 2.2–2.4 μm range too red to be consistent with HIP 21152 B. Hence, we estimate the most-likely spectral type of the companion to be T1.5 $^{+0.5}_{-1.0}$, which is a slightly later type than HD 33632 Ab (L9.5 $^{+1.0}_{-3.0}$; Currie et al. 2020a). Following Stephens et al. (2009), HIP 21152 B’s spectral-type range implies an effective temperature of $T_{\text{eff}} \sim 1200\text{--}1300$ K, similar to the 1200–1400 K temperature estimated for HD 33632 Ab. The relationship between the bolometric correction in the H band (BC_H) and spectral type from Liu et al. (2010) provides $BC_H = 2.56^{+0.07}_{-0.07}$ for HIP 21152 B. Assuming a solar bolometric magnitude of 4.74 (Willmer 2018) and the distance of 43.208 $^{+0.050}_{-0.049}$ pc for the HIP 21152 system (Bailer-Jones et al.

2021), the companion’s bolometric luminosity is then $\log(L/L_\odot) = -4.673 \pm 0.066$.

4. Astrometric Analysis

4.1. HIP 21152 B Astrometry

We measured the projected separations (ρ in units of milliarcseconds) and the position angles (PAs) of HIP 21152 B relative to its central star by fitting elliptical Gaussian models to the companion PSFs identified in all the ALOCI-processed images. For the CHARIS images, the PSF-fitting was conducted in the images after median-combining all the wavelength channels. Forward modeling allowed us to assess astrometric biasing due to processing. Table 1 shows the HIP 21152 B astrometry. The astrometric errors were estimated by taking into account contributions from noise including speckle residuals, calibration errors on the plate scales and true-north angles of the instruments we used, and systematic errors in the measurements of the primary star’s absolute centers (see Appendix D.1 for details and the error budgets).

HIP 21152 B’s motion is inconsistent with the relative motion of a background object expected from the astrometry information of the central star from Gaia EDR3 (Gaia Collaboration et al. 2021): The measured versus predicted

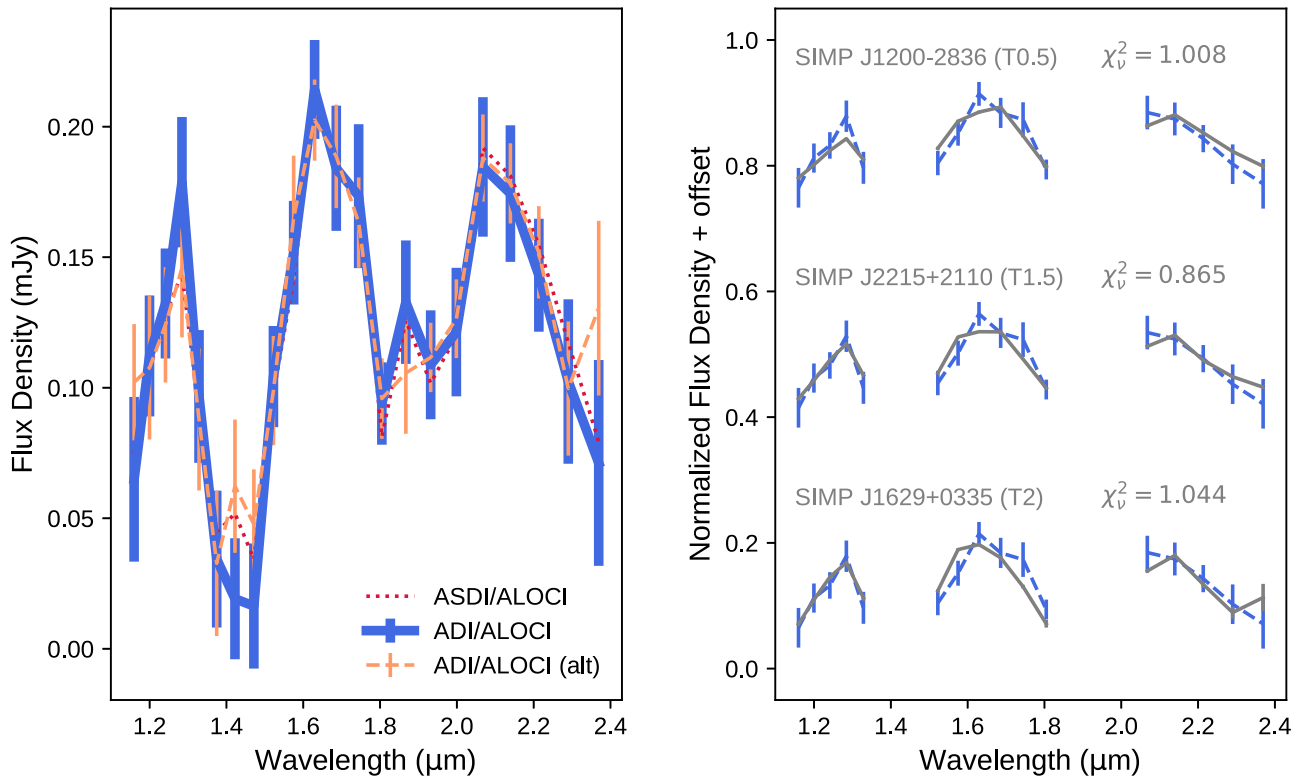


Figure 3. The 2020 October *JHK* spectra of HIP 21152 B. (Left) The three lines correspond to the fiducial ADI, ASDI, and alternate ADI (labeled as “alt”) reductions. 1σ error bars are appended to the ADI spectra. (Right) Comparisons between the fiducial spectrum of HIP 21152 B (blue dashed lines) and three template spectra from the Montreal Spectral Library (gray solid lines). The wavelengths where telluric absorption is significant are masked and were not used in our spectral typing. The reduced chi-square values (χ^2_v) computed by least-squares fitting (15 DOF = 16 data points minus 1 optimized parameter for spectrum scaling) are shown above each comparison with the names of the compared BDs and their spectral types.

position in 2021 October differs by more than 10σ in both ρ and PA (see also Appendix D.2).

4.2. Orbit and Dynamical Mass Estimates

To constrain HIP 21152 B’s orbit and dynamical mass, we model the star’s absolute astrometry from HGCA (without the use of epoch astrometry), the star’s RV measurements, and the companion’s relative astrometry from direct imaging using the *orvara* software (Brandt et al. 2021). Our *orvara* analysis carries out Markov Chain Monte Carlo (MCMC) simulations by adopting 15 temperatures in the parallel tempering chain and 100 walkers. Each chain has 7×10^5 steps; we save every 25th step for 28,000 steps per walker. We assume a Gaussian prior for the stellar mass: Its mean and standard deviation are set to be 1.3 and $0.1 M_\odot$ following David & Hillenbrand (2015). For the other parameters, our fit assumed the default priors of *orvara* including the $1/M$ prior for the companion’s mass (Brandt et al. 2021; see also Appendix D.2). RV jitter was simulated in the range of $0\text{--}100 \text{ m s}^{-1}$ with a log-flat prior. We discarded the initial 2500 steps as the burn-in phase from the recorded 28,000 steps. With 100 walkers, we have 2.55×10^6 samples for inference.

Figure 4 shows the corner plot of the fitted system parameters from *orvara*, predicted orbits, and predicted RVs (see Appendix D.2 for the fits to the other measurements). The median and the 16th–84th percentiles of the MCMC posteriors are provided in Appendix D.2. HIP 21152 B has a best-fit semimajor axis (a) of $17.5^{+7.2}_{-3.8}$ au, viewed at a high inclination of $i = 104.8^{+15.0}_{-6.9}^\circ$. The estimated mass of the primary

largely reflects our input prior, while the companion’s mass was estimated to be $27.8^{+8.4}_{-5.4} M_{\text{Jup}}$. We find no strong constraints on the eccentricity (e) of the companion posterior.

5. Discussion

We directly imaged a substellar companion orbiting ~ 18 au from the Sun-like star HIP 21152, which has an accelerating proper motion. The companion’s spectrum is best reproduced by an object near the L/T transition, plausibly an early T dwarf. The system is a member of the Hyades open cluster (OC), which has a well-constrained age of 750 ± 100 Myr. It is notable that there have been reports of single BDs (e.g., Lodieu et al. 2019) and BD binaries (e.g., Duchêne et al. 2013) directly imaged in this OC. In contrast, there has been no unequivocal confirmation of directly imaged companions that are less massive than the hydrogen-burning limit (e.g., Fernandes et al. 2019) around main-sequence stars in Hyades (see a note in Appendix E).

Accordingly, HIP 21152 B is a crucial benchmark to understand substellar-mass objects as below. HIP 21152 B’s dynamical mass is approximately twice the deuterium-burning limit and at/slightly above the estimated turnover in mass separating massive Jovian exoplanets from BDs (Sahlmann et al. 2011). Table 1 in Fransson et al. (2022) lists all the ages and dynamical masses of directly imaged substellar companions. We can compare those companions with HIP 21152 B, which has a fractional age uncertainty of 13% ($100 \text{ Myr}/750 \text{ Myr}$). Smaller fractional uncertainties in age estimations lead to smaller fractional uncertainties in mass estimations for directly

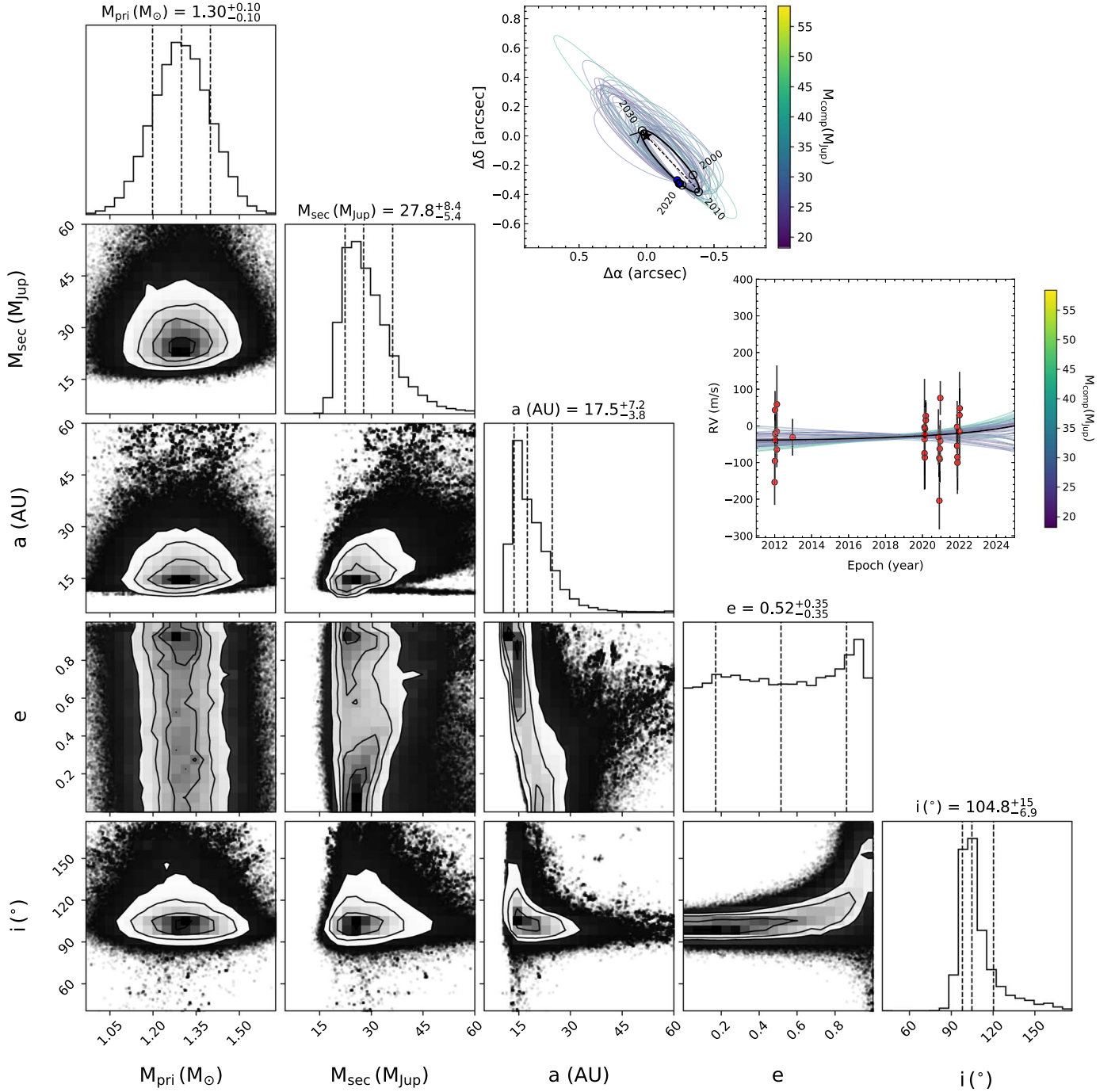


Figure 4. Corner plot showing MCMC posterior distributions of the host-star mass (M_{pri} in units of M_{\odot}), companion mass (M_{sec} in units of M_{Jup}), semimajor axis (a), eccentricity (e), and inclination (i). HIDES RV measurements of HIP 21152 A (lower inset) and relative astrometry of HIP 21152 B from CHARIS and NIRC2 (upper inset) are shown, with the best-fit orbit (black solid line) along with 100 orbits randomly taken from our MCMC chains that are color-coded by HIP 21152 B’s mass corresponding to the color bars near the inset panels. See also Appendix D.2 for the fitting results to the other measurements.

imaged substellar companions. For example, the models of Baraffe et al. (2003) convert a luminosity of $\log(L/L_{\odot}) \approx -4.9$ to $8 \pm 1 M_{\text{Jup}}$ ($26 \pm 4 M_{\text{Jup}}$) at an age of 50 ± 10 Myr (500 ± 100 Myr); meanwhile, the same luminosity corresponds to $8 \pm 2 M_{\text{Jup}}$ ($26^{+6}_{-7} M_{\text{Jup}}$) at 50 ± 20 Myr (500 ± 200 Myr). The corresponding fractional uncertainties for all cases in the list of Franson et al. (2022) are larger than 16%, except for the planets around β Pic, which are 13% just as for HIP 21152 B. Furthermore, the majority (11/18) of the companions have fractional uncertainties higher than $\sim 30\%$. Thus, the smallest

fractional age uncertainty of HIP 21152 B provides the highest-fidelity model-dependent mass estimations, besides β Pic bc.

In the list, β Pic bc and HR 8799 e are the only directly imaged giant planets whose masses have been dynamically constrained. HIP 21152 B is the closest to those benchmark planets in terms of dynamical mass, best helping unveil the physical and chemical connection between giant planets and BDs. We note that only HIP 21152 B is firmly associated with an OC among these benchmark substellar companions. The

methods used to characterize stellar and substellar objects such as age estimation techniques (e.g., Mamajek & Hillenbrand 2008) and evolutionary models (e.g., Tognelli et al. 2020) have been calibrated by the observations of OCs. The Hyades OC is especially useful for such calibrations due to its proximity to the Sun. Hence, HIP 21152 B would be available as one of the best benchmark companions to test evolution and atmosphere theories of cool objects among directly imaged BDs with inferred dynamical masses.

In contrast to the dynamical mass, given HIP 21152 B's bolometric luminosity of $\log(L/L_{\odot}) = -4.673 \pm 0.066$ and a system age of $\approx 650\text{--}850$ Myr, the Baraffe et al. (2003) luminosity-evolution models yield slightly higher predicted masses of $33\text{--}42 M_{\text{Jup}}$. However, temperatures implied by this age range— $1200\text{--}1350$ K—are broadly consistent with spectroscopically derived values. Thus, HIP 21152 B may provide another example of $1\sigma\text{--}2\sigma$ tension between substellar dynamical masses and those inferred from luminosity evolution at intermediate ages. Dupuy et al. (2009, 2014) found significant discrepancies between the dynamical masses and luminosity-evolution-inferred masses for the BD binaries GJ 417 BC and HD 130948 BC. Both systems have ages comparable to Hyades members but have masses of $\approx 50 M_{\text{Jup}}$, or $\sim 50\%$ higher than HIP 21152 B. Future astrometric monitoring of HIP 21152 B will further test whether luminosity evolution models can overestimate the masses of substellar objects.

HIP 21152 B is a benchmark to test atmosphere models of substellar objects as well. For instance, gravity-sensitive absorption features such as KI and FeH can be measured via medium- to high-resolution spectroscopy (e.g., Martin et al. 2017). Those measurements allow the comparison of HIP 21152 B's surface gravity estimated by atmosphere models with that constrained by its dynamical mass and radius (which is appropriately assumed to be about $0.1 R_{\odot}$ at Hyades's age; Baraffe et al. 2003). It is also interesting to characterize HIP 21152 B in the context of the L/T transition of substellar objects depending on surface gravity and metallicity (e.g., Faherty et al. 2012). HIP 21152 B benefits such a characterization as an anchor point, due to a supersolar metallicity expected from its membership to the Hyades OC (Gagné et al. 2018; Gossage et al. 2018) and the semiempirically constrained surface gravity.

HIP 21152 B's companion-to-primary mass ratio, q , is $\sim 2.0\%^{+0.7\%}_{-0.4\%}$. This value is intermediate between bona fide directly imaged exoplanets like HR 8799 bcde (e.g., Marois et al. 2008; Currie et al. 2014) and BD companions imaged around Sun-like stars such as HD 33632 Ab (Currie et al. 2020a) and HD 47127 B (Bowler et al. 2021). Very few binary-star companions have mass ratios this low (Kraus et al. 2008); surveys suggest that the substellar-mass function turns over at a mass ratio of $q \sim 0.025$, where lower (higher) mass ratio companions may be best interpreted as exoplanets (BDs).

In OCs, the gravitational interactions of passing stars can perturb companions on wide orbits and cause ejections in some cases. Fujii & Hori (2019) explored the ejection of planets by modeling stellar encounters in OCs via N -body simulations. They found that ejections do not frequently occur in a low-density OC like the Hyades, even in cases where planets orbit their hosts at semimajor axes of $10\text{--}100$ au. Their findings should be applicable also to low-mass-ratio companions like HIP 21152 B and consistent with this discovery, contributing to

the verification of such a theory for the dynamics of planet/BD companions in OCs.

Finally, this discovery provides further evidence of the promise of using precision astrometry to select direct-imaging targets. Even for a system 750 ± 100 Myr old, we were able to directly detect a $\approx 20\text{--}30 M_{\text{Jup}}$ companion orbiting on solar system scales with high S/Ns, demonstrating the capability of extreme AO instruments to detect cooler companions at $10\text{--}20 M_{\text{Jup}}$ on the same scale. A large sample of directly imaged exoplanets and BDs with high-quality spectra, dynamical masses, and well-constrained ages will clarify how atmospheres of substellar objects evolve depending on the companion mass and how they link to their formation mechanisms.

We thank Zhoujian Zhang for discussions about bolometric correction, Michiko Fujii for stellar encounters in open clusters, and Brendan Bowler for the companion of 1RXS J034231.8 +121622. This work has made use of data from the European Space Agency (ESA) mission Gaia (Gaia Collaboration et al. 2016; <https://www.cosmos.esa.int/gaia>), processed by the Gaia Data Processing and Analysis Consortium (DPAC, <https://www.cosmos.esa.int/web/gaia/dpac/consortium>). Funding for the DPAC has been provided by national institutions, in particular the institutions participating in the Gaia Multilateral Agreement. This publication makes use of data products from the Two Micron All Sky Survey, which is a joint project of the University of Massachusetts and the Infrared Processing and Analysis Center/California Institute of Technology, funded by the National Aeronautics and Space Administration and the National Science Foundation. For the Keck-II/NIRC2 data (P.I. T. Currie), this research has made use of the Keck Observatory Archive (KOA), which is operated by the W. M. Keck Observatory and the NASA Exoplanet Science Institute (NExSci), under contract with the National Aeronautics and Space Administration. This work has benefited from The UltracoolSheet, maintained by Will Best, Trent Dupuy, Michael Liu, Rob Siverd, and Zhoujian Zhang, and developed from compilations by Dupuy & Liu (2012), Dupuy & Kraus (2013), Liu et al. (2016), Best et al. (2018), and Best et al. (2021). This research has benefited from the Montreal Brown Dwarf and Exoplanet Spectral Library, maintained by Jonathan Gagné. This research has made use of the SIMBAD and VizieR services, both operated at Centre de Données astronomiques de Strasbourg (CDS, <https://cds.u-strasbg.fr/>) in France, and NASA's Astrophysics Data System Bibliographic Services. IRAF is distributed by the National Optical Astronomy Observatories, which is operated by the Association of Universities for Research in Astronomy, Inc. (AURA) under cooperative agreement with the National Science Foundation. Part of the data analysis was carried out on the Multi-wavelength Data Analysis System operated by the Astronomy Data Center (ADC), National Astronomical Observatory of Japan.

We are honored and grateful for the opportunity of observing the universe from Maunakea, which has cultural, historical, and natural significance in Hawaii. We appreciate the critical support from all the current and recent Subaru and Keck Observatory staff. Their support was essential in achieving this discovery, especially amidst the many difficulties associated with the COVID-19 pandemic.

We thank the Subaru and NASA Keck Time Allocation Committees for their generous support of this program. T.C.

was supported by a NASA Senior Postdoctoral Fellowship and NASA/Keck grant LK-2663-948181. T.B. gratefully acknowledges support from the Heising-Simons Foundation and from NASA under grant No. 80NSSC18K0439. V.D. and N.S. were supported by the NASA grant Nos. 80NSSC19K0336. K.A. also gratefully acknowledges support from the Heising-Simons Foundation. K.W. acknowledges support from NASA through the NASA Hubble Fellowship grant HST-HF2-51472.001-A awarded by the Space Telescope Science Institute, which is operated by the Association of Universities for Research in Astronomy, Incorporated, under NASA contract NAS5-26555. Part of this work was carried out at the Jet Propulsion Laboratory, California Institute of Technology, under contract with NASA. The results reported herein benefited from collaborations and/or information exchange within NASA’s Nexus for Exoplanet System Science (NExSS) research coordination network sponsored by NASA’s Science Mission Directorate. M.T. is supported by JSPS KAKENHI grant No. 18H05442, and E.A. is supported by MEXT/JSPS KAKENHI grant No. 17K05399.

The development of SCEXAO was supported by JSPS (Grant-in-Aid for Research Nos. 23340051, 26220704, 23103002, and 21H04998), Astrobiology Center of NINS, the Mt Cuba Foundation, and the director’s contingency fund at Subaru Telescope. CHARIS was developed under the support of the Grant-in-Aid for Scientific Research on Innovative Areas No. 2302. The Okayama 188 cm telescope is operated by a consortium led by the Exoplanet Observation Research Center, Tokyo Institute of Technology (Tokyo Tech), under the framework of tripartite cooperation among Asakuchi-city, NAOJ, and Tokyo Tech. This research is based on data collected at the Subaru Telescope, which is operated by the National Astronomical Observatory of Japan. Some of the data presented herein were obtained at the W. M. Keck Observatory, which is operated as a scientific partnership among the California Institute of Technology, the University of California and the National Aeronautics and Space Administration. The Observatory was made possible by the generous financial support of the W. M. Keck Foundation.

Facility: the Subaru Telescope (SCEXAO, CHARIS), Keck: II (NIRC2).

Software: `astropy` (Astropy Collaboration et al. 2013, 2018), `BANYAN-Σ` (Gagné et al. 2018), `CHARIS-DRP` (Brandt et al. 2017), `CHARIS-DPP` (<https://github.com/thaynecurrie/charis-dpp>, Currie et al. 2020b), `orvara` (Brandt et al. 2021), `IRAF` : (Tody et al. 1986, 1993), `matplotlib` (Hunter 2007), `numpy` (van der Walt et al. 2011), `scipy` (Virtanen et al. 2020), `sympy` (Meurer et al. 2017), `pandas` (McKinney 2010), `Google Colaboratory`.

Appendix A

Details of the High-contrast Image Processing

We here describe the specific considerations that were taken during our data reductions for high-contrast imaging. Poor-

quality data cubes needed to be removed because they affect the data reduction procedure. In order to remove poor Strehl-ratio CHARIS data cubes, we processed only the data with peak-to-halo ratios greater than 10, which are the signal ratios of satellite-spot peaks relative to halos of the central star PSFs. This criterion led us to exclude 8 (3%) and 69 (35%) data cubes from observations obtained in October and December of 2020, respectively. The 2021 October data are split into two sequences, between which the wind-driven halo changed direction: Cubes from one sequence are poorly correlated with the other. For these data, we retain the first sequence because the AO performance and the change in parallactic angle are better (35 data cubes removed).

For all data sets, we spatially filtered the data using a radial-profile subtraction and subtracted the speckle halo using the ALOCI-ADI algorithm (Currie et al. 2014, 2018). For the CHARIS data of 2020 October and December, we truncated the set of reference images for each target image based on the correlation between every target-reference pair, selecting the 120 and 100 best-correlated reference images, respectively. We did not apply this truncation due to the processing of the data from 2021 October due to the small number of available exposures. Other algorithm parameters defining the geometry over which we optimized our reference PSF construction and subtracted this PSF were varied but were generally close to pipeline default values: an optimization area (in units of PSF footprints) of $N_A = 100$ and a rotation gap of 0.5–0.75 the FWHM of the PSF (see, e.g., Pueyo et al. 2012).

To further explore speckle suppression, we considered two additional approaches. First, for CHARIS data, we also applied an SDI reduction on the post-ADI residuals as performed in Currie et al. (2018), which improves speckle suppression but may introduce less reliable spectral extractions (Pueyo et al. 2012). Due to the worse observing conditions in 2021 October, our analysis relies on SDI reductions for this epoch. Second, we made alternate ADI reductions that are different from the main procedures, using a proprietary version of ALOCI for which modifications included varying the optimization/subtraction zone geometries and turning on/off a pixel mask over the subtraction zone. With the adoption of pixel masking, linear-combination coefficients for reference PSF construction are calculated after masking the pixels in PSF subtraction zones. This technique has been used elsewhere (e.g., Pueyo et al. 2012; Currie et al. 2018) including in the public ALOCI pipeline to suppress a bias from companion PSFs and significant self-subtractions; indeed, we obtained better throughputs using this technique. Meanwhile, the proprietary version of ALOCI has the option to adopt several types of optimization zone shapes, including the standard shape that has been commonly used (e.g., Pueyo et al. 2012), and optimize the zone geometry.

Appendix B Supplemental Information for Spectroscopy

B.1. Spectroscopy from 2020 December Data

Inspection of the 2020 December data showed issues with spectrophotometric calibration that impeded our ability to extract a spectrum with a quality comparable to that obtained from the 2020 October data. Using our default ALOCI-ADI reduction, we measure broadband photometry of $J = 18.29 \pm 0.42$, $H = 17.15 \pm 0.19$, and $K_s = 16.16 \pm 0.16$ mag. While the H -band photometry in 2020 October and December is consistent within 1σ , the J - and K_s -band measurements are discrepant at the 1.2σ and 1.7σ levels. As shown in Figure 5 (left panel), the differences in spectra between the 2020 October and 2020 December ADI reductions are significantly larger than the error bars in the shortest and (especially) longest wavelength channels.

Further investigation of this issue identified some partial mitigation measures. The alternate ADI/ALOCI reduction using pixel masking and a different optimization zone geometry yields better agreement (Figure 5 left panel), suggesting that contamination from residual speckles may be affecting the K -band measurements.

We also note that the measured spectrum from the 2020 December data can be affected by the nonuniform brightnesses of the satellite spots adopted in the spectrophotometric calibration. The satellite spots in the 2020 December cubes showed modest brightness differences in a channel ($2.37 \mu\text{m}$), while they show smaller brightness differences at $1.58 \mu\text{m}$ (Figure 6). The 2020 December satellite spots show the spot-to-spot nonuniformity larger ($\sim 10\%$) than the 2020 October spots only in the $2.37 \mu\text{m}$ channels (Figure 6) and telluric-dominated channels, whereas the spots should have roughly equal

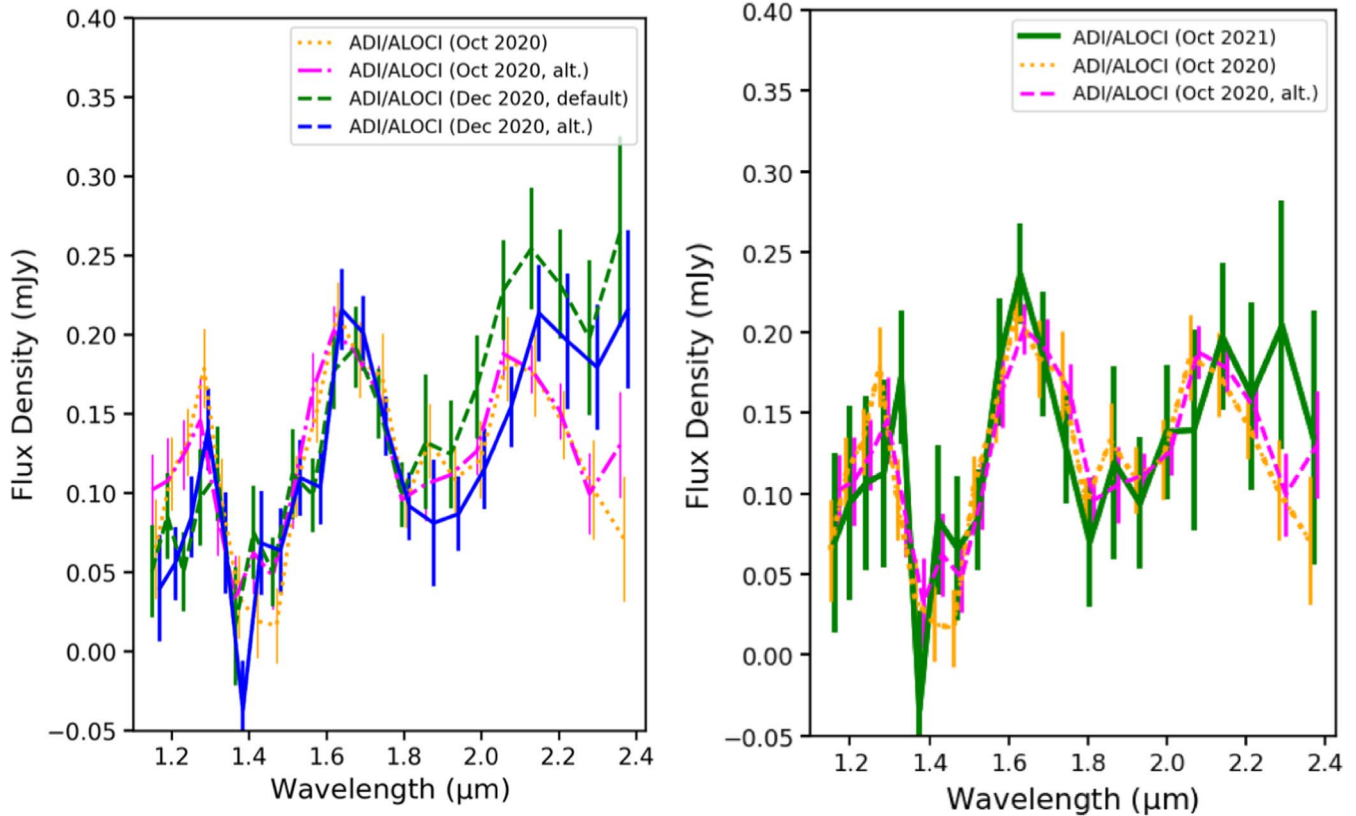


Figure 5. (Left) Comparison between the 2020 October spectra and 2020 December spectra extracted using different reduction approaches. (Right) October 2021 spectrum compared to spectra extracted from 2020 October data. In both the left and right panels, “alt” indicates the alternative ALOCI-ADI reductions. The spectral wavelengths of the spectra on the left and right panels are slightly shifted to avoid plot overlap.

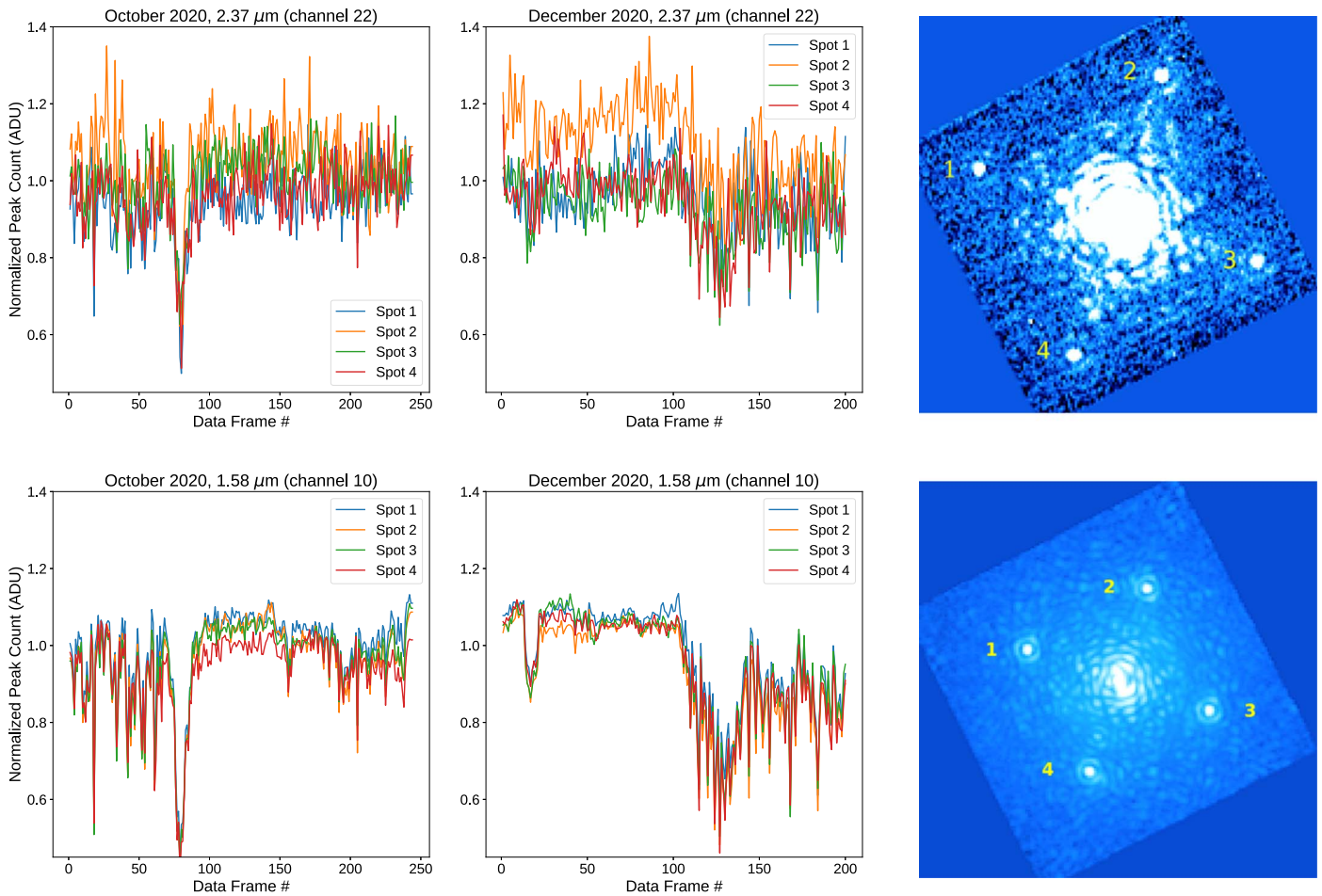


Figure 6. Normalized peak count of satellite spots in the reddest wavelength ($2.37 \mu\text{m}$) and $1.58 \mu\text{m}$ slices for cubes in the 2020 October (left) and 2020 December (middle) data. The right-hand panels label the satellite spots.

brightness, yielding spectrophotometric precision on the order of $\sim 2\%$ (Currie et al. 2020b).

Given the apparent problems with the 2020 December data and the higher quality of the 2020 October data, we adopt the 2020 October spectrum as the basis for our analysis.³⁸ The lower PSF qualities of the 2020 December images are also implied by the larger number of data that we needed to omit (see Appendix A) and the more unstable systematic variations of satellite-spot brightness (see Figure 6). We note that the $J - K_s$ colors for the 2020 December spectra derived from the alternate ADI reduction are $J - K_s = 1.60 \pm 0.35$ with an apparent J -band magnitude of 18.05 ± 0.29 (absolute J -band magnitude of 14.87 ± 0.29). The resulting color–magnitude diagram positions also lie at the L/T transition as was found in our analyses of the 2020 October spectrum. Thus, any uncertainties in the shape of HIP 21152 B’s spectrum at red wavelengths have a negligible impact on our broad conclusions about HIP 21152 B as a substellar object at the L/T transition.

B.2. Spectroscopy from 2021 October Data

The right panel of Figure 5 compares the spectrum extracted from our 2021 October data set to that taken a year prior. Overall, the 2021 spectrum is noisier at all wavelengths but

Table 2
HIP 21152 B Spectrum

Wavelength (μm)	F_ν (mJy)	σF_ν (mJy)	S/N
1.160	0.065	0.032	2.1
1.200	0.112	0.023	5.0
1.241	0.132	0.021	6.5
1.284	0.179	0.025	8.0
1.329	0.097	0.025	3.9
1.375	0.034	0.026	1.3
1.422	0.019	0.023	0.8
1.471	0.016	0.024	0.7
1.522	0.104	0.019	5.6
1.575	0.152	0.02	8.2
1.630	0.214	0.019	12.2
1.686	0.184	0.024	9.1
1.744	0.173	0.028	7.0
1.805	0.094	0.016	6.5
1.867	0.133	0.024	5.9
1.932	0.109	0.021	5.5
1.999	0.121	0.025	5.1
2.068	0.185	0.027	8.8
2.139	0.174	0.026	7.7
2.213	0.143	0.022	7.6
2.290	0.102	0.031	3.3
2.369	0.071	0.039	1.8

³⁸ The October 2021 data are too low in S/N to clarify the true spectrum of HIP 21152 B, though they are consistent with the 2020 October results (see Appendix B.2).

Note. Throughput-corrected HIP 21152 B spectrum extracted from 2020 October 7 data, reduced using the ADI/ALOCI pipeline for SCEXAO/CHARIS.

agrees in both absolute flux density and shape with the 2020 October results. New spectra extracted from higher-S/N data and taken at higher resolution are required to advance our understanding of HIP 21152 B's spectral properties.

B.3. HIP 21152 B Spectrum

In Table 2 below, we present the HIP 21152 B spectrum derived from our standard ALOCI-ADI reduction of the 2020 October data.

Appendix C Radial-velocity Measurements of HIP 21152

In Table 3, we list individual relative RV measurements for HIP 21152.

Table 3
Relative Radial-Velocity Measurements of HIP 21152

JD (days)	RV	σ_{RV}
2455926.0892653	-121.3	62.0
2455933.0817933	-63.4	51.8
2455933.9964362	75.7	51.9
2455934.9652493	-6.2	52.9
2455936.0063207	11.3	52.2
2455967.0789619	17.2	58.2
2455969.0504358	-31.9	48.5
2455970.0574695	91.4	105.8
2456281.1998284	1.6	50.2
2458890.9400706	-42.1	99.4
2458890.9510289	28.8	132.0
2458893.9469028	-4.1	53.4
2458896.9166423	9.1	73.8
2458896.9275914	-53.6	84.9
2458899.9304815	24.7	61.2
2458916.9258056	59.5	41.8
2458916.9367650	47.9	48.3
2459166.1754479	2.0	75.9
2459185.0422269	-171.7	78.4
2459185.0531852	-54.9	51.1
2459192.9858299	-58.3	62.8
2459192.9967882	-30.1	64.1
2459204.0201065	108.4	46.2
2459204.0310602	-8.9	56.9
2459537.1362429	29.8	70.7
2459537.1468725	-21.9	86.4
2459543.2202619	-52.5	100.8
2459543.2313550	-68.0	75.5
2459584.1654891	61.7	118.2
2459586.0721793	16.2	79.2
2459588.0634205	17.0	59.4
2459588.0744923	80.5	54.7

Note. The measured RVs and their errors are given in units of m s^{-1} .

Appendix D

Supplemental Information for Astrometric Analysis

D.1. Empirical Analysis of Relative Astrometry Measurements

As CHARIS was craned in and out of position multiple times between our observations, we reassessed the plate scale and true-north orientation angle offset of the CHARIS detector. As in Currie et al. (2018, 2020a), we used the SCEXAO/CHARIS and Keck II/NIRC2 data of the companion around HD 1160 to identify any change in detector astrometric properties.³⁹ As described in Currie et al. (2022), these analyses favor a slightly revised plate scale of 16.15 ± 0.05 mas pixel⁻¹ but otherwise no measurable changes in the astrometric calibration determined in Currie et al. (2018). Our analysis is based on the revised pixel scale described above, and the true-north orientation offset angle in Currie et al. (2018). Contemporaneous CHARIS and NIRC2 astrometry for the HD 1160's companion find consistent results: e.g., $\rho = 0''.791$ and $0''.797$; position angle (PA) = $244^\circ 60$ and $244^\circ 80$ for high-quality 2020 October and lower-quality 2020 December CHARIS data compared to $\rho = 0''.791$, PA = $244^\circ 79$ for high-quality NIRC2 data. Our NIRC2 astrometric measurements are based on the distortion calibration of Service et al. (2016), from which we adopt the plate scale of 9.971 ± 0.004 mas pixel⁻¹ and the true-north orientation offset of $0^\circ 262 \pm 0^\circ 020$.

We also consider an absolute astrometric error due to uncertainties in determining the star's positions. For the Keck/NIRC2 data, Konopacky et al. (2016) quote an uncertainty of ~ 2 mas in the star's center when determined through the partially transmissive Lyot coronagraph. For CHARIS, internal source tests described in Currie et al. (2020b) included analyses of the star position determined from fitting the satellite spots versus unobstructed PSF centroids. The tests reveal up to a 0.25 pixel offset (~ 4 mas) in the reported position of the centroid estimated from satellite spots and that determined from an unobstructed PSF. The NKT Photonics SuperK laser we used for this analysis only extends to $1.7 \mu\text{m}$, so we do not have a direct measurement of any biasing at longer wavelengths. The source of this difference is unclear but could be due to residual field distortion. As an empirical test, we compared the centroid positions for HD 1160's companion in seven different data sets from 2020 August to 2022 January, a timeframe over which we expect the orbital motion to be negligible as in Currie et al. (2018); the standard deviation in the east and north positions are ~ 3.7 and ~ 2.3 mas. To be conservative, we adopt an absolute astrometric error in each coordinate of 0.25 pixels ($= 4$ mas) for CHARIS.

For CHARIS, the uncertainties from astrometric biasing due to processing and (for the 2020 October and December data sets) the intrinsic detection S/Ns are small compared to the intrinsic uncertainties in the pixel scale (0.05 mas), north position angle offset ($0^\circ 27$), and absolute centroid measurement (~ 4 mas). However, residual and only partially whitened speckle noise may contaminate centroid measurements more than expected from an S/N estimate (e.g., as in Gaspar & Rieke 2020). We simulated noise-injected companion PSFs to estimate the random uncertainties of the companion centroids in the CHARIS images, providing an empirically motivated estimate of our centroid uncertainties. The simulated PSFs were made by adding noise floors to the forward-modeled PSFs (see

Section 2.1 and Currie et al. 2018). The noise floors were taken from the areas in the final images created by combining the PSF-subtracted cube frames. Then, we used the areas at the same separations as the companion but the different 12 PAs, which start from the companion's PA + 45° and end at the companion's PA + 320° with intervals of 25° . The standard deviations of the centroids calculated from the simulated PSFs were taken to be the random uncertainties of the companion centroid measurements. These uncertainties [σ_x , σ_y] are equal to [0.074, 0.109], [0.133, 0.081], and [0.18, 0.17] pixels ($=$ [1.2, 1.8], [2.1, 1.3], and [2.9, 2.8] mas with a plate scale of 16.15 mas pixel⁻¹) for the 2020 October, 2020 December, and 2021 October CHARIS images. We do not perform the same analysis for the NIRC2 L' data because the S/N is lower and the intrinsic PSF is roughly twice as large as CHARIS's ($\theta \approx 0''.08$ versus $0''.043$). In this case, the centroid uncertainty estimated from the intrinsic S/N is ~ 0.35 pixels—significantly larger than for any CHARIS measurement.

Another source of the random errors is attributed to the alignment of the individual images. We evaluated this error source using the SCEXAO/CHARIS data sets obtained in 2020 October and December for HIP 21152. The residuals between the central star's positions calculated at each wavelength channel of a cube and the polynomial function fit to the positions can correspond to the image alignment errors. The residual scatter of an image alignment is much smaller than the other insignificant error sources (see above) and further decreases when integrating all frames and all channels; we thus ignore the image alignment errors in SCEXAO/CHARIS. Table 4 summarizes the error evaluations described above for the CHARIS measurements. When the astrometric calibrations for SCEXAO/CHARIS will be updated in the future (e.g., for distortion calibration), we recommend the reader refer to Table 4 to recalculate the astrometric measurements with the updated calibrations.

D.2. Common Proper Motion and Orbit Analysis

In Figure 7, we compare the measured positions of HIP 21152 B relative to HIP 21152 A with the positions expected if HIP 21152 B is an unbound background object (i.e., common proper-motion analysis). The expectation was made with HIP 21152 A's right ascension (R.A.), decl. (decl.), R.A. and decl. proper motions, and parallax from Gaia EDR3 (Gaia Collaboration et al. 2021). The results from our `orvara` orbit modeling for the HIP 21152 system (Section 4.2) are summarized in Table 5. In addition to Figure 4, Figure 8 shows the fitted orbits to HIP 21152 A's proper-motion

Table 4
HIP 21152 B Relative Astrometry Uncertainties in CHARIS Without Systematic Errors of 0.25 Pixels (see Appendix D.1)

Date (UT)	Instrument	[σ_x , σ_y] (pixels)	σ_ρ (mas)	σ_{PA} ($^\circ$)
2020-10-07	SCEXAO/CHARIS	[0.074, 0.109]	2.0	0.34
2020-12-04	SCEXAO/CHARIS	[0.133, 0.081]	2.1	0.38
2021-10-14	SCEXAO/CHARIS	[0.18, 0.17]	3.0	0.51

Note. Angular separations are in units of milliarcseconds. The calibration errors in the CHARIS plate scale and true-north orientation offset are included in σ_ρ and σ_{PA} .

³⁹ This analysis is described in full in an upcoming paper (A. Torres-Quijado & T. Currie et al. 2022, in preparation).

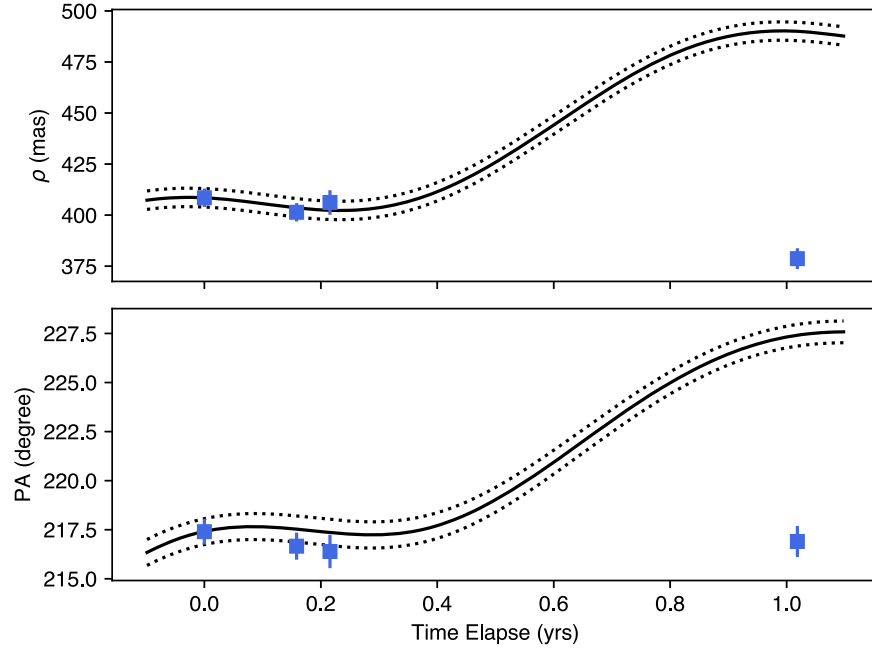


Figure 7. Common proper-motion analysis for HIP 21152 B. The projected separation (ρ) and position angle (PA) measurements for HIP 21152 B are shown at the top and bottom panels, respectively. The horizontal axes indicate the time elapsed from the 2020 October epoch. An expected motion assuming HIP 21152 B is a background star is shown by the solid lines encompassed by their 1σ errors (dashed lines). It is clearly demonstrated that HIP 21152 B cannot be a background star given the large difference between the expected background motion and the measured ρ and PA at the latest epoch (October 2021): 16σ in ρ and 11σ in PA.

Table 5
MCMC Orbit-fitting Results

Parameter	Median and 16th–84th Percentile Fitted parameters	95% Credible Interval	Prior
RV jitter (m s^{-1})	$<0.013^a$	(0.0, 12.1)	$1/\sigma_{\text{jit}}$ (log-flat)
$M_{\text{pri}} (M_{\odot})$	$1.30_{-0.10}^{+0.10}$	(1.10, 1.49)	$\mathcal{N}(1.3, 0.1)$
$M_{\text{sec}} (M_{\text{Jup}})$	$27.8_{-5.4}^{+8.4}$	(19.2, 49.9)	$1/M_{\text{sec}}$ (log-flat)
a (au)	$17.5_{-3.8}^{+7.2}$	(12.4, 38.0)	$1/a$ (log-flat)
$\sqrt{e} \sin \omega$	$0.09_{-0.42}^{+0.39}$	(−0.62, 0.73)	uniform
$\sqrt{e} \cos \omega$	$0.29_{-0.85}^{+0.52}$	(−0.90, 0.95)	uniform
Inclination ($^{\circ}$)	$104.8_{-6.9}^{+15}$	(92.2, 155.5)	$\sin i$ ($i=0-180$)
PA of ascending node Ω ($^{\circ}$)	$49.4_{-8.0}^{+17.0}$	(36.8, 228)	uniform
Mean longitude at 2010.0 ($^{\circ}$)	188_{-49}^{+60}	(5, 355)	uniform
Parallax (mas) ^b	$23.109_{-0.028}^{+0.028}$	(23.052, 23.166)	$\mathcal{N}(\varpi_{\text{Gaia}}, \sigma_{\varpi, \text{Gaia}})$
Derived parameters			
Orbital period (yr)	63_{-20}^{+43}	(38, 203)	
Argument of periastron ω ($^{\circ}$)	157_{-132}^{+179}	(4, 357)	
Eccentricity e	0.52 ± 0.35	(0.03, 0.97)	
Semimajor axis (mas)	404_{-89}^{+167}	(286, 878)	
Periastron time T_0 (JD − 2400000)	63360_{-1419}^{+5307}	(58700, 93300)	
Mass ratio	$0.0204_{-0.0040}^{+0.0065}$	(0.014, 0.037)	

Notes. $\mathcal{N}(\mu, \sigma)$ represents a Gaussian with mean μ and variance σ^2 .

^a The maximum likelihood RV jitter is zero.

^b The uncertainty includes the Gaia uncertainty (Gaia Collaboration et al. 2021) in quadrature with the standard deviation in maximum likelihood parallaxes from the chains.

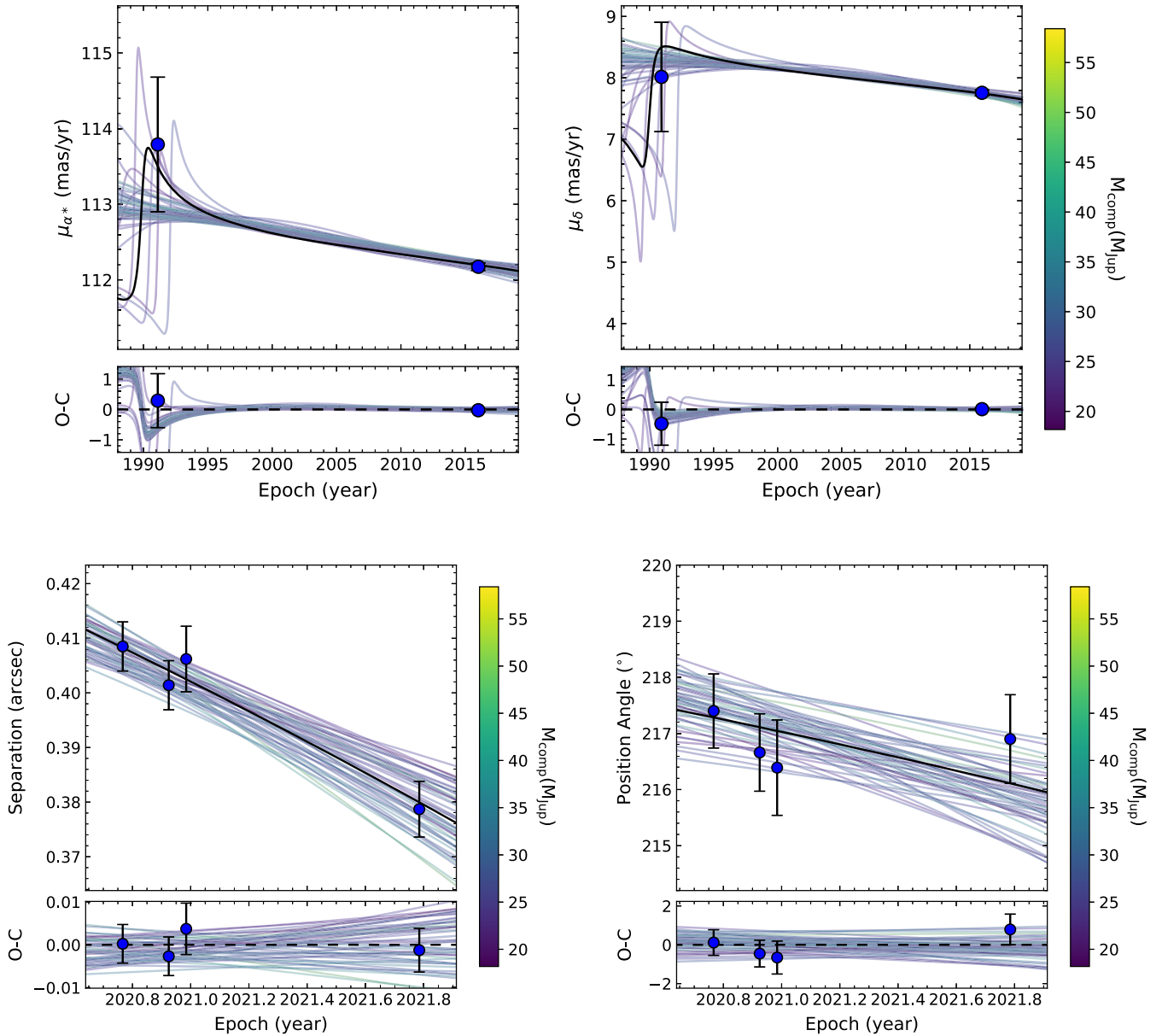


Figure 8. HIP 21152 A’s proper-motion variations along R.A. (top left) and decl. (top right) and the measured projected separations (bottom left) and position angles (PAs; bottom right) of HIP 21152 B relative to HIP 21152 A. The best-fit orbit is indicated by black solid curves, while the 100 randomly selected orbits are shown by color-coded curves. The color bars near each panel correspond to the companion’s mass.

variations from HGCA (Brandt 2021) along the R.A. and decl. and HIP 21152 B’s projected separations and position angles.

Appendix E

Substellar Companion Candidates around Main-sequence Stars in the Hyades

There have been no previous reports of confirmed substellar companions to main-sequence stars in the Hyades OC, despite its proximity to the solar system. We note that Morzinski et al. (2012) reported candidates of Hyades substellar companions detected with shallow adaptive optics imaging. In addition, an $L1 \pm 1$ -type companion around the M4-type star 1RXS J034231.8+121622 was reported by Bowler et al. (2015). A similarity in the space velocities and the sky position of this system with those of the Hyades OC was already discussed in Bowler et al. (2015); nevertheless, they concluded that this

system’s membership to the Hyades OC is unclear. For 1RXS J034231.8+121622, we run the Banyan- Σ algorithm (Gagné et al. 2018) with the star’s distance adopted in Bowler et al. (2015); R.A., decl., and proper-motion measurements from Gaia Collaboration et al. (2021); and absolute RV from Shkolnik et al. (2012), giving a zero probability of being a Hyades member. In contrast, we compute a membership probability for the same star of 99.9% using the same algorithm after updating the distance to a Gaia-based measurement from Bailer-Jones et al. (2021); the different membership probability is therefore caused by Gaia data becoming available. Although 1RXS J034231.8+121622 B can be identified as a high-probability member of the Hyades OC, it is still unclear whether the companion has a substellar mass. We calculate a mass of 1RXS J034231.8+121622 B with the new membership and the Gaia-based distance measurement. For this companion,


we adopt a distance of $32.96_{-0.024}^{+0.022}$ pc from Bailer-Jones et al. (2021) and calculate an H -band bolometric correction of 2.70 ± 0.08 mag following Liu et al. (2010) to convert an H -band apparent magnitude of 13.51 ± 0.05 (Bowler et al. 2015) to the bolometric luminosity of $\log(L/L_{\odot}) = -3.552 \pm 0.038$. With the age of Hyades (750 ± 100 Myr) and the evolutionary models of Baraffe et al. (2003), the bolometric luminosity is converted to a mass of $76\text{--}83 M_{\text{Jup}}$, which is near or slightly above the hydrogen-burning limit ($\approx 70\text{--}80 M_{\text{Jup}}$ in general; e.g., Fernandes et al. 2019). We thus find that 1RXS J034231.8 +121622 B is a candidate substellar companion in the Hyades OC.

ORCID iDs

Masayuki Kuzuhara  <https://orcid.org/0000-0002-4677-9182>

Thayne Currie  <https://orcid.org/0000-0002-7405-3119>

Timothy D. Brandt  <https://orcid.org/0000-0003-2630-8073>

Taichi Uyama  <https://orcid.org/0000-0002-6879-3030>

Markus Janson  <https://orcid.org/0000-0001-8345-593X>

Jeffrey Chilcote  <https://orcid.org/0000-0001-6305-7272>

Taylor Tobin  <https://orcid.org/0000-0001-8103-5499>

Kellen Lawson  <https://orcid.org/0000-0002-6964-8732>

Yasunori Hori  <https://orcid.org/0000-0003-4676-0251>

Olivier Guyon  <https://orcid.org/0000-0002-1097-9908>

Tyler D. Groff  <https://orcid.org/0000-0001-5978-3247>

Julien Lozi  <https://orcid.org/0000-0002-3047-1845>

Sebastien Viedard  <https://orcid.org/0000-0003-4018-2569>

Ananya Sahoo  <https://orcid.org/0000-0003-2806-1254>

Vincent Deo  <https://orcid.org/0000-0003-4514-7906>

Nemanja Jovanovic  <https://orcid.org/0000-0001-5213-6207>

Kyohoon Ahn  <https://orcid.org/0000-0002-1094-852X>

Frantz Martinache  <https://orcid.org/0000-0003-1180-4138>

Nour Skaf  <https://orcid.org/0000-0002-9372-5056>

Eiji Akiyama  <https://orcid.org/0000-0002-5082-8880>

Barnaby R. Norris  <https://orcid.org/0000-0002-8352-7515>


Mickaël Bonnefoy  <https://orcid.org/0000-0001-5579-5339>

Krzysztof G. Helminiak  <https://orcid.org/0000-0002-7650-3603>

Tomoyuki Kudo  <https://orcid.org/0000-0002-9294-1793>

Michael W. McElwain  <https://orcid.org/0000-0003-0241-8956>

Matthias Samland  <https://orcid.org/0000-0001-9992-4067>

Kevin Wagner  <https://orcid.org/0000-0002-4309-6343>

John Wisniewski  <https://orcid.org/0000-0001-9209-1808>

Gillian R. Knapp  <https://orcid.org/0000-0002-9259-1164>

Jungmi Kwon  <https://orcid.org/0000-0003-2815-7774>

Jun Nishikawa  <https://orcid.org/0000-0001-9326-8134>

Masahiko Hayashi  <https://orcid.org/0000-0002-4790-7940>

Motohide Tamura  <https://orcid.org/0000-0002-6510-0681>

References

Astropy Collaboration, Price-Whelan, A. M., Sipőcz, B. M., et al. 2018, *AJ*, 156, 123

Astropy Collaboration, Robitaille, T. P., Tollerud, E. J., et al. 2013, *A&A*, 558, A33

Bailer-Jones, C. A. L., Rybizki, J., Fousneau, M., Demleitner, M., & Andrae, R. 2021, *AJ*, 161, 147

Baraffe, I., Chabrier, G., Barman, T. S., Allard, F., & Hauschildt, P. H. 2003, *A&A*, 402, 701

Best, W. M. J., Dupuy, T. J., Liu, M. C., Siverd, R. J., & Zhang, Z. 2020, The UltracoolSheet: Photometry, Astrometry, Spectroscopy, and Multiplicity for

3000+ Ultracool Dwarfs and Imaged Exoplanets, 1.0.0, Zenodo, doi:10.5281/zenodo.4169085

Best, W. M. J., Liu, M. C., Magnier, E. A., & Dupuy, T. J. 2021, *AJ*, 161, 42

Best, W. M. J., Magnier, E. A., Liu, M. C., et al. 2018, *ApJS*, 234, 1

Bonavita, M., Fontanive, C., Gratton, R., et al. 2022, *MNRAS*, 513, 5588

Bond, C. Z., Cetre, S., Lilley, S., et al. 2020, *JATIS*, 6, 039003

Bowler, B. P., Endl, M., Cochran, W. D., et al. 2021, *ApJL*, 913, L26

Bowler, B. P., Liu, M. C., Shkolnik, E. L., & Tamura, M. 2015, *ApJS*, 216, 7

Brandt, T. D. 2018, *ApJS*, 239, 31

Brandt, T. D. 2021, *ApJS*, 254, 42

Brandt, T. D., Dupuy, T. J., Li, Y., et al. 2021, *AJ*, 162, 186

Brandt, T. D., & Huang, C. X. 2015, *ApJ*, 807, 58

Brandt, T. D., Rizzo, M., Groff, T., et al. 2017, *JATIS*, 3, 048002

Carpenter, J. M. 2001, *AJ*, 121, 2851

Castelli, F., & Kurucz, R. L. 2003, in IAU Symp. 210, Modelling of Stellar Atmospheres, ed. N. Piskunov, W. W. Weiss, & D. F. Gray (San Francisco: ASP)

Currie, T., Burrows, A., Girard, J. H., et al. 2014, *ApJ*, 795, 133

Currie, T., Burrows, A., Itoh, Y., et al. 2011, *ApJ*, 729, 128

Currie, T., Brandt, T. D., Kuzuhara, M., et al. 2020a, *ApJL*, 904, L25

Currie, T., Brandt, T. D., Uyama, T., et al. 2018, *AJ*, 156, 291

Currie, T., Guyon, O., Lozi, J., et al. 2020b, *Proc. SPIE*, 11448, 114487H

Currie, T., Lawson, K., Schneider, G., et al. 2022, *NatAs*, 6, 751

David, T. J., & Hillenbrand, L. A. 2015, *ApJ*, 804, 146

De Rosa, R. J., Rameau, J., Patience, J., et al. 2016, *ApJ*, 824, 121

Duchêne, G., Bouvier, J., Moraux, E., et al. 2013, *A&A*, 555, A137

Dupuy, T. J., & Kraus, A. L. 2013, *Sci*, 341, 1492

Dupuy, T. J., & Liu, M. C. 2012, *ApJS*, 201, 19

Dupuy, T. J., Liu, M. C., & Ireland, M. J. 2009, *ApJ*, 692, 729

Dupuy, T. J., Liu, M. C., & Ireland, M. J. 2014, *ApJ*, 790, 133

Faherty, J. K., Burgasser, A. J., Walter, F. M., et al. 2012, *ApJ*, 752, 56

Fernandes, C. S., Van Grootel, V., Salmon, S. J. A. J., et al. 2019, *ApJ*, 879, 94

Franson, K., Bowler, B. P., Brandt, T. D., et al. 2022, *AJ*, 163, 50

Fujii, M. S., & Hori, Y. 2019, *A&A*, 624, A110

Gagné, J., Faherty, J. K., Cruz, K. L., et al. 2015, *ApJS*, 219, 33

Gagné, J., Mamajek, E. E., Malo, L., et al. 2018, *ApJ*, 856, 23

Gaia Collaboration, Brown, A. G. A., Vallenari, A., et al. 2021, *A&A*, 649, A1

Gaia Collaboration, Prusti, T., de Bruijne, J. H. J., et al. 2016, *A&A*, 595, A1

Gaspar, A., & Rieke, G. 2020, *PNAS*, 117, 9712

Gossage, S., Conroy, C., Dotter, A., et al. 2018, *ApJ*, 863, 67

Greco, J. P., & Brandt, T. D. 2016, *ApJ*, 833, 134

Groff, T. D., Chilcote, J., Kasdin, N. J., et al. 2016, *Proc. SPIE*, 9908, 99080O

Hayano, Y., Takami, H., Guyon, O., et al. 2008, *Proc. SPIE*, 7015, 70151O

Hoffleit, D. 1964, Catalogue of Bright Stars (3rd ed.; New Haven, CT: Yale Univ. Press)

Hunter, J. D. 2007, *CSE*, 9, 90

Janson, M., Brandt, T. D., Kuzuhara, M., et al. 2013, *ApJL*, 778, L4

Jovanovic, N., Martinache, F., Guyon, O., et al. 2015, *PASP*, 127, 890

Kambe, E., Yoshida, M., Izumiura, H., et al. 2013, *PASJ*, 65, 15

Kenyon, S. J., & Hartmann, L. 1995, *ApJS*, 101, 117

Kepler, M., Benisty, M., Müller, A., et al. 2018, *A&A*, 617, A44

Konopacky, Q. M., Marois, C., Macintosh, B. A., et al. 2016, *AJ*, 152, 28

Kraus, A. L., Ireland, M. J., Martinache, F., & Lloyd, J. P. 2008, *ApJ*, 679, 762

Kuzuhara, M., Tamura, M., Kudo, T., et al. 2013, *ApJ*, 774, 11

Lagrange, A. M., Bonnefoy, M., Chauvin, G., et al. 2010, *Sci*, 329, 57

Leggett, S. K., Burningham, B., Saumon, D., et al. 2010, *ApJ*, 710, 1627

Liu, M. C., Dupuy, T. J., & Allers, K. N. 2016, *ApJ*, 833, 96

Liu, M. C., Dupuy, T. J., & Leggett, S. K. 2010, *ApJ*, 722, 311

Lodieu, N., Smart, R. L., Pérez-Garrido, A., & Silvotti, R. 2019, *A&A*, 623, A35

Macintosh, B., Graham, J. R., Barman, T., et al. 2015, *Sci*, 350, 64

Mamajek, E. E., & Hillenbrand, L. A. 2008, *ApJ*, 687, 1264

Marois, C., Macintosh, B., Barman, T., et al. 2008, *Sci*, 322, 1348

Martin, E. C., Mace, G. N., McLean, I. S., et al. 2017, *ApJ*, 838, 73

Mawet, D., Milli, J., Wahhaj, Z., et al. 2014, *ApJ*, 792, 97

McKinney, W. 2010, in Proc. of the 9th Python in Science Conf., ed. S. van der Walt & J. Millman, 56

Metchev, S., Marois, C., & Zuckerman, B. 2009, *ApJL*, 705, L204

Meurer, A., Smith, C. P., Paprocki, M., et al. 2017, *PeerJ Comput. Sci.*, 3, e103

Morzinski, K. M., Macintosh, B. A., Close, L. M., et al. 2012, *Proc. SPIE*, 8447, 84470O

Nielsen, E. L., De Rosa, R. J., Macintosh, B., et al. 2019, *AJ*, 158, 13

Oppenheimer, B. R., & Hinkley, S. 2009, *ARA&A*, 47, 253

Pueyo, L., Crepp, J. R., Vasisht, G., et al. 2012, *ApJS*, 199, 6

Rajan, A., Rameau, J., De Rosa, R. J., et al. 2017, *AJ*, 154, 10

- Robert, J., Gagné, J., Artigau, É., et al. 2016, *ApJ*, 830, 144
- Sahlmann, J., Ségransan, D., Queloz, D., et al. 2011, *A&A*, 525, A95
- Sahoo, A., Guyon, O., Lozi, J., et al. 2020, *AJ*, 159, 250
- Sato, B., Kambe, E., Takeda, Y., Izumiura, H., & Ando, H. 2002, *PASJ*, 54, 873
- Sato, B., Omiya, M., Harakawa, H., et al. 2012, *PASJ*, 64, 135
- Service, M., Lu, J. R., Campbell, R., et al. 2016, *PASP*, 128, 095004
- Shkolnik, E. L., Anglada-Escudé, G., Liu, M. C., et al. 2012, *ApJ*, 758, 56
- Skemer, A. J., Marley, M. S., Hinz, P. M., et al. 2014, *ApJ*, 792, 17
- Skrutskie, M. F., Cutri, R. M., Stiening, R., et al. 2003, 2MASS All-Sky Point Source Catalog, IPAC, doi:10.26131/IRSA2
- Skrutskie, M. F., Cutri, R. M., Stiening, R., et al. 2006, *AJ*, 131, 1163
- Stephens, D. C., Leggett, S. K., Cushing, M. C., et al. 2009, *ApJ*, 702, 154
- Tody, D. 1986, *Proc. SPIE*, 627, 733
- Tody, D. 1993, in ASP Conf. Ser. 52, *Astronomical Data Analysis Software and Systems II*, ed. R. J. Hanisch, R. J. V. Brissenden, & J. Barnes (San Francisco, CA: ASP), 173
- Tognelli, E., Dell’Omodarme, M., Valle, G., Prada Moroni, P. G., & Degl’Innocenti, S. 2020, *MNRAS*, 501, 383
- van der Walt, S., Colbert, S. C., & Varoquaux, G. 2011, *CSE*, 13, 22
- Virtanen, P., Gommers, R., Oliphant, T. E., et al. 2020, *NatMe*, 17, 261
- Willmer, C. N. A. 2018, *ApJS*, 236, 47
- Zurlo, A., Vigan, A., Galicher, R., et al. 2016, *A&A*, 587, A57